

Comparison of turbulence-induced scintillations for multi-wavelength laser beacons over tactical (7 km) and long (149 km) atmospheric propagation paths

M. Vorontsov¹, V. S. Rao Gudimetla², G. Carhart³, T. Weyrauch¹, S. Lachinova⁴, E. Polnau¹, J. Reiersen¹, L. Beresnev³, J. Liu³, and J. F. Riker⁵

1. University of Dayton, School of Engineering, 300 College Park College Park Center, LOCI, Dayton, OH, 45469-2951
2. U. S. Air Force Research Laboratory, Directed Energy Directorate, Det. 15, 535 Lipoa Parkway, Khehe, HI 96753
3. U. S. Army Research Laboratory, 2600 Powder Mill Road, Adelphi. MD, 20783
4. Optonicus LLC, 711 E. Monument Ave. Suite 101, Dayton, OH 45402
5. U. S. Air Force Research Laboratory, Space Vehicles Directorate, 3550 Aberdeen Ave SE, Kirtland AFB, NM 87117

ABSTRACT

We report results of the experimental analysis of atmospheric effects on laser beam propagation over two distinctive propagation paths: a long-range (149 km) propagation path between Mauna Loa (Island of Hawaii) and Haleakala (Island of Maui) mountains, and a tactical-range (7 km) propagation path between the roof of the Dayton Veterans Administration Medical Center (VAMC) and the Intelligent Optics Laboratory (IOL/UD) located on the 5th floor of the University of Dayton College Park Center building. Both testbeds include three laser beacons operating at wavelengths 532 nm, 1064 nm, and 1550 nm and a set of identical optical receiver systems with fast-framing IR cameras for simultaneous measurements of pupil and focal plane intensity distributions. The results reported here are focused on analysis of intensity scintillations that were simultaneously measured at three wavelengths. Comparison of experimental results shows significant differences in the physics of atmospheric turbulence impact on laser beam propagation over the long- and tactical-range distances.

1. INTRODUCTION

In this paper we continue analysis (see ref. [1]) of the experimental data obtained during the Coherent Multi-Beam Atmospheric Transceiver (COMBAT) experiments performed in February 2010 using a 149 km long near-horizontal atmospheric path between a laser beacon platform located on Mauna Loa peak and the 3.67 m AMOS receiver telescope at the summit of Haleakala in the Hawaii Islands. For comparison of atmospheric turbulence impact on laser beam propagation over considerably different distances, we also included results of more recent laser beam propagation experiments using a 7 km long near-horizontal path.

The COMBAT experimental campaign provided a large amount of intensity scintillation data that were obtained by utilizing multi-wavelength laser beacons. In these experiments intensity scintillations were simultaneously measured using three closely (6 cm apart) located identical laser beacons that generated truncated (<8% of total energy) Gaussian beams at the following wavelengths: $\lambda_1 = 0.53 \mu\text{m}$, $\lambda_2 = 1.06 \mu\text{m}$, and $\lambda_3 = 1.55 \mu\text{m}$. The COMBAT experimental setting and measurement techniques are described in [1]. After completion of the long-range experiments the COMBAT system was relocated to the IOL at the University of Dayton and re-assembled using a 7 km propagation path with the beacon platform located on the roof of the Dayton VA Medical Center (VAMC) and the sensing modules positioned on the 5th floor of the UD College Park Center building.

In this paper we compare results of intensity scintillation measurements performed over the 149 km and the 7 km atmospheric propagation paths using identical experimental settings. These two experiments are referred to here as long- and tactical-range COMBAT settings or COMBAT/LR and COMBAT/TR.

Report Documentation Page

Form Approved
OMB No. 0704-0188

Public reporting burden for the collection of information is estimated to average 1 hour per response, including the time for reviewing instructions, searching existing data sources, gathering and maintaining the data needed, and completing and reviewing the collection of information. Send comments regarding this burden estimate or any other aspect of this collection of information, including suggestions for reducing this burden, to Washington Headquarters Services, Directorate for Information Operations and Reports, 1215 Jefferson Davis Highway, Suite 1204, Arlington VA 22202-4302. Respondents should be aware that notwithstanding any other provision of law, no person shall be subject to a penalty for failing to comply with a collection of information if it does not display a currently valid OMB control number.

1. REPORT DATE SEP 2011	2. REPORT TYPE	3. DATES COVERED 00-00-2011 to 00-00-2011	
4. TITLE AND SUBTITLE Comparison of turbulence-induced scintillations for multi-wavelength laser beacons over tactical (7 km) and long (149 km) atmospheric propagation paths		5a. CONTRACT NUMBER	
		5b. GRANT NUMBER	
		5c. PROGRAM ELEMENT NUMBER	
6. AUTHOR(S)		5d. PROJECT NUMBER	
		5e. TASK NUMBER	
		5f. WORK UNIT NUMBER	
7. PERFORMING ORGANIZATION NAME(S) AND ADDRESS(ES) Air Force Research Laboratory, Space Vehicles Directorate, 3550 Aberdeen Dr SE, Kirtland AFB, NM, 87117		8. PERFORMING ORGANIZATION REPORT NUMBER	
9. SPONSORING/MONITORING AGENCY NAME(S) AND ADDRESS(ES)		10. SPONSOR/MONITOR'S ACRONYM(S)	
		11. SPONSOR/MONITOR'S REPORT NUMBER(S)	
12. DISTRIBUTION/AVAILABILITY STATEMENT Approved for public release; distribution unlimited			
13. SUPPLEMENTARY NOTES AMOS, Advanced Maui Optical and Space Surveillance Technologies Conference, 12-16 Sep 2011, Maui, HI.			
14. ABSTRACT We report results of the experimental analysis of atmospheric effects on laser beam propagation over two distinctive propagation paths: a long-range (149 km) propagation path between Mauna Loa (Island of Hawaii) and Haleakala (Island of Maui) mountains, and a tactical-range (7 km) propagation path between the roof of the Dayton Veterans Administration Medical Center (VAMC) and the Intelligent Optics Laboratory (IOL/UD) located on the 5th floor of the University of Dayton College Park Center building. Both testbeds include three laser beacons operating at wavelengths 532 nm, 1064 nm, and 1550 nm and a set of identical optical receiver systems with fast-framing IR cameras for simultaneous measurements of pupil and focal plane intensity distributions. The results reported here are focused on analysis of intensity scintillations that were simultaneously measured at three wavelengths. Comparison of experimental results shows significant differences in the physics of atmospheric turbulence impact on laser beam propagation over the long- and tactical-range distances.			
15. SUBJECT TERMS			
16. SECURITY CLASSIFICATION OF:			17. LIMITATION OF ABSTRACT
a. REPORT unclassified	b. ABSTRACT unclassified	c. THIS PAGE unclassified	
			18. NUMBER OF PAGES 9
			19a. NAME OF RESPONSIBLE PERSON

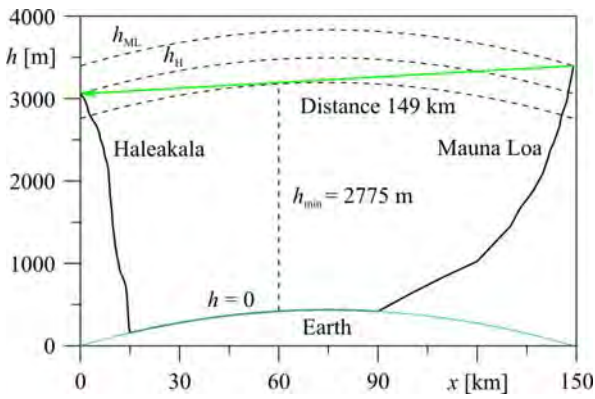


Fig. 1. Elevation profile along the propagation path from the Mauna Loa NOAA observatory to the AFRL AEOS telescope on Haleakala in the long-range COMBAT experimental setting (left) and snapshot of the 3.67 m AEOS receiver telescope (right) taken during the COMBAT/LR experiment. The telescope is illuminated by the green ($\lambda_1 = 0.53 \mu\text{m}$) laser beacon. The photo provides a rough estimation of the beam footprint of approximately 10 m in diameter.

2. COMBAT EXPERIMENTAL SETTINGS

The propagation geometries of both long- and tactical-range COMBAT settings are shown in Figs. 1 and 2. In the COMBAT/LR setting in Fig. 1 the laser beacon platform was located on Mauna Loa mountain at elevation $h_{ML} = 3397 \text{ m}$ (11,140 ft), and the 3.67-m receiver telescope at the summit of Haleakala at elevation $h_H = 3058 \text{ m}$. In the COMBAT/TR setting in Fig. 2 the beacon platform was located on an optical table inside a shed that was anchored to concrete slabs on the roof of VA medical center building. In both experimental settings, the laser beacon assembly was comprised of three single-mode fiber collimators (each with a clear aperture of 26 mm) and the corresponding fiber-coupled laser diodes at wavelengths of $\lambda_1 = 0.532 \mu\text{m}$, $\lambda_2 = 1.064 \mu\text{m}$ and $\lambda_3 = 1.55 \mu\text{m}$. For technical reasons only two laser beacons with wavelengths $\lambda_1 = 0.532 \mu\text{m}$ and $\lambda_2 = 1.064 \mu\text{m}$ were used in the COMBAT/TR experiments described here. The fiber collimators were mounted together with an aiming telescope in a gimbal system (see Fig. 3) with a smallest angular step size of $1.75 \mu\text{rad}$ that was used for alignment. After propagation to the receiver site (3.67 m AEOS telescope at Haleakala in the COMBAT/LR setting, or 0.35 m Schmidt-Cassegrain telescope just beyond the IOL window in the COMBAT/TR system), optical waves from the

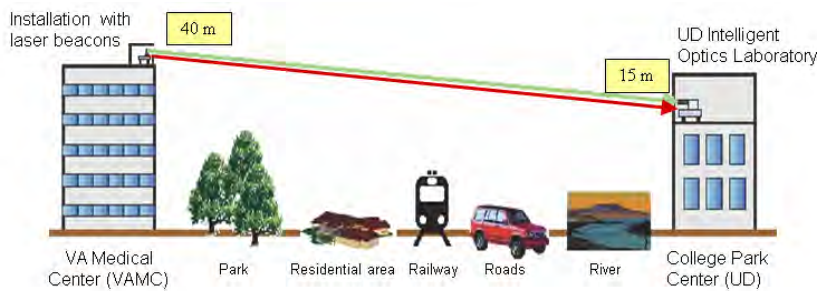


Fig. 2. Graphical representation of the 7 km long atmospheric propagation path in the tactical-range COMBAT experimental setting (left) and snapshot of green laser beacon image taken from the receiver site at IOL/UD (window on the 5th floor of the College Park Center building). The beacon platform was located at elevation 40 m, while COMBAT/TR optical receiver system at elevation 15 m.

beacons were received by the telescopes and demagnified by corresponding optical relay systems. The resulting collimated beam of diameter 10 cm (in both COMBAT settings) was subdivided into separate subapertures, each having a usable diameter of 25 mm, and sent to the receiver modules as shown in Fig. 3 and Fig. 4. Each subaperture corresponds to an area with a diameter of 91.7 cm at the telescope pupil for the long-range and 8.5 cm for the tactical-range COMBAT settings. The angular dimension of the corresponding receiver subapertures are $6.1 \mu\text{rad}$ for the COMBAT/LR and $12.1 \mu\text{rad}$ for the COMBAT/TR settings. Three separate subapertures in the long-range sensing system and a single sub-aperture in the tactical-range setting were used to record pupil-plane and focal-plane irradiance distributions of the received beams as shown in Fig. 3. Narrow bandpass filters were used to dedicate each receiver module to a specific wave from a single beacon. In this paper we discuss only measurements of the pupil-plane intensity distributions, which were recorded using three Sensors Unlimited (SU640SDWHvis) 14-

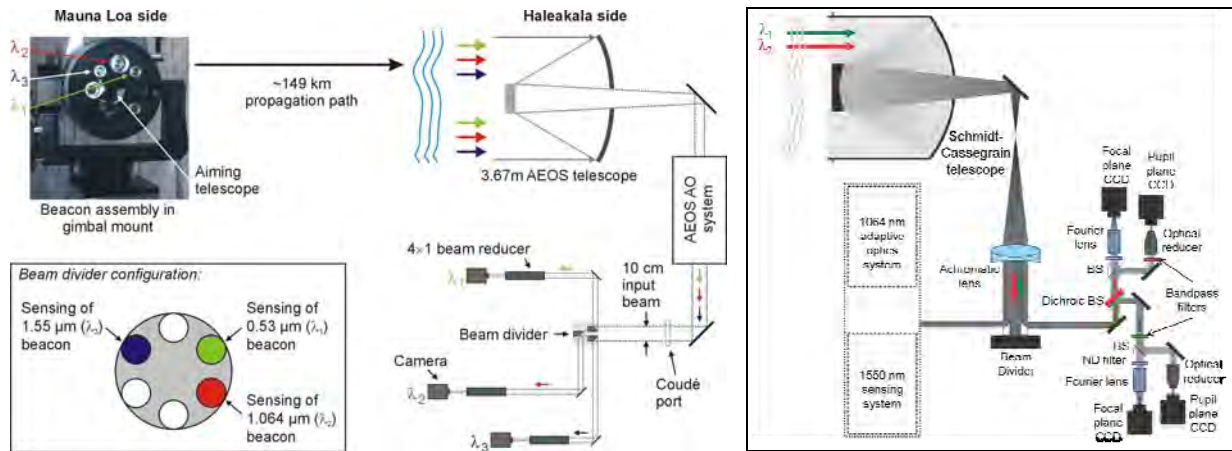


Fig. 3. Conceptual schematics of the long-range (left) and tactical range (right) COMBAT experimental settings. The identical beacon assembly (shown at left upper corner) and the pupil and focal plane sensing modules (shown at right) were used in both COMBAT systems. The adaptive optics and 1550 nm sensing modules in the COMBAT/TR system were not included in the experiments described.

bit cameras. The cameras were operating in a windowed mode with a 256×256 pixel window with pixel size of $25 \times 25 \mu\text{m}^2$, providing an actual sensor area of $6.4 \times 6.4 \text{ mm}^2$ and a 100% fill factor. A four-to-one beam reducer was installed in the optical train of each subaperture to match the beam (pupil) size with the active window size.

3. MEASUREMENTS AND RESULTS

3.1 Short-exposure Intensity Scintillation Patterns. Characteristic snapshots of the received light pupil-plane intensity distributions for beacons with different wavelengths measured in both COMBAT experiments are illustrated in Fig. Error! Reference source not found.. The images show that the spatial scale of intensity scintillations is strongly dependent on the wavelength, i.e., the longer the wavelength the larger the atmospheric effects induced intensity speckles. This observation is consistent with the theoretical findings and was also confirmed by our numerical simulations. At the same time intensity scintillation patterns for the long-range (first

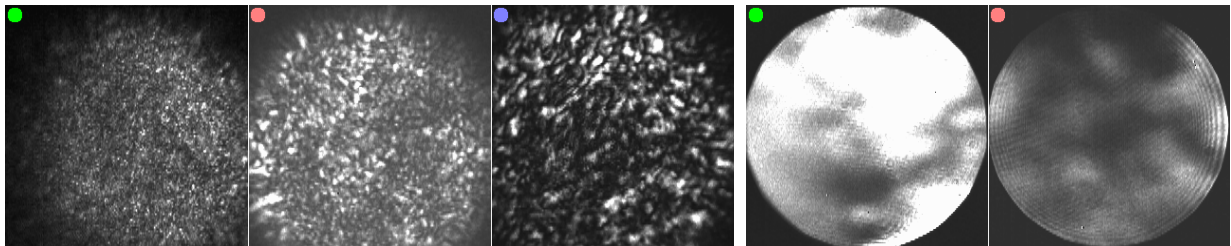


Fig. 4. Characteristic examples of the short-exposure intensity scintillation patterns recorded during the long-range (three photos from left to right) and tactical-range (two photos at right) COMBAT experiments. The beacon wavelength is identified by color of small circles at left upper corner of each photograph: green circle corresponds to $\lambda_1 = 0.532 \mu\text{m}$, red to $\lambda_2 = 1.064 \mu\text{m}$ and blue to $\lambda_3 = 1.55 \mu\text{m}$.

three images at right) and the tactical-range propagation distances are profoundly different despite the fact that in both cases the ratios of the beam footprint (for $\lambda_1 = 0.53 \mu\text{m}$) to receiver aperture diameter were nearly equal in both experimental settings. These ratios are 10.9 for COMBAT/LR and 10.6 for COMBAT/TR. The characteristic speckle size in the intensity images for $\lambda_1 = 0.53 \mu\text{m}$ in Fig. 4 are 5-10 mm for 149 km and 17-20 mm for 7 km propagation distances.

3.2 Received Power Fluctuations and Giant Spikes. Consider characteristic examples of temporal dynamics of the received light power measured inside the 91.7 cm aperture for the long-range and 8.5 cm aperture for the tactical-range COMBAT settings. The power fluctuations data were simultaneously recorded for three beacons in the long-range and for two (for $\lambda_1 = 0.53 \mu\text{m}$ and for $\lambda_2 = 1.06 \mu\text{m}$) beacons in tactical-range experiments. The

dependencies of the normalized power $\hat{P}(n)$ on the consequent short-exposure pupil-plane frame number n are shown in Fig. 5 for the long-range and in Fig. 6 for the tactical-range experiments. In both cases the received power was normalized by the maximum value corresponding to each experiment. As can be seen from these figures, dynamics of receiver power fluctuations are quite different for 149 km and 7 km propagation paths. The long-range

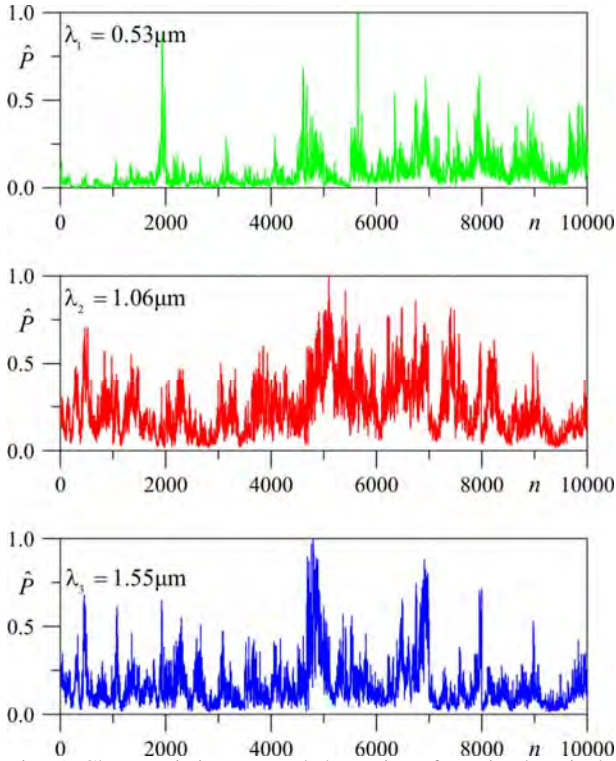


Fig. 5. Characteristic temporal dynamics of received optical power fluctuations $\hat{P} = P_n / \max_n P_n$ for laser beacons with wavelengths $\lambda_1 = 0.53 \mu\text{m}$ (top), $\lambda_2 = 1.06 \mu\text{m}$ (middle), and $\lambda_3 = 1.55 \mu\text{m}$ (bottom) obtained in the long-range experiments. All three sequences of 10000 short-exposure frames with 2 ms integration time and frame rate 200 f/sec were captured simultaneously.

short duration (on the order of 5-20 ms) of spikes cannot be directly associated with atmospheric processes that occur over a significantly longer time scale.

As a possible physical explanation for the formation of these giant spikes, we consider the trapping of the beacon beam inside a relatively narrow stratified layer of air with sharp changes of refractive index at its boundaries. Such a layer can act as a wave-guide – similar to the way an optical fiber acts with respect to an optical beam with wavelength matched to the fiber core size. This wave-guiding effect is extremely sensitive to the wavelength of the propagating beam and the coupling angle and can be destroyed with small variation of the stratified layer geometry or of the angle of optical wave incidence. These small variations can indeed occur at a time scale of the duration of the observed spikes.

propagation results in appearance of large spikes in the received power that were absent in the experiments performed over the tactical-range distance.

These giant spikes, each lasting for only a few milliseconds, result in up to ten-fold increase in received power. Note that in the experiments in Fig. 5 the amplitude of spikes appeared to be significantly higher for $\lambda_1 = 0.53 \mu\text{m}$. At the same time in a different set of experiments the largest amplitude of the spikes were observed at different wavelengths. For example Fig. 7 shows results of a different set of experiments with the largest amplitude spikes observed at $\lambda_3 = 1.55 \mu\text{m}$. The giant spikes appeared quite randomly with a characteristic delay time of the order of a few seconds. This time scale can be associated with changes occurring in coherent atmospheric structures and/or with the dynamics of stable (refractive) and unstable (turbulent) layers aligned with the Earth curvature that the beacon beams propagate through. On the other hand, the extremely

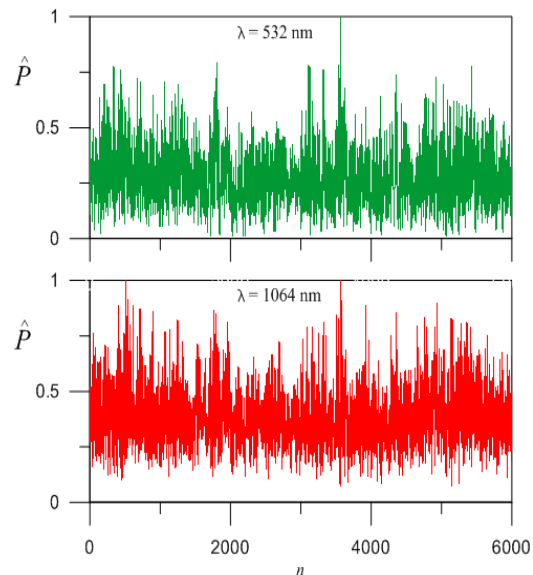


Fig. 6. Characteristic temporal dynamics of received optical power fluctuations $\hat{P} = P_n / \max_n P_n$ for laser beacons with wavelengths $\lambda_1 = 0.53 \mu\text{m}$ (top) and $\lambda_2 = 1.06 \mu\text{m}$ (bottom) obtained in the tactical-range experiments. Sequences of 6000 short-exposure frames with 2 ms integration time and frame rate 200 fr/sec were captured simultaneously.

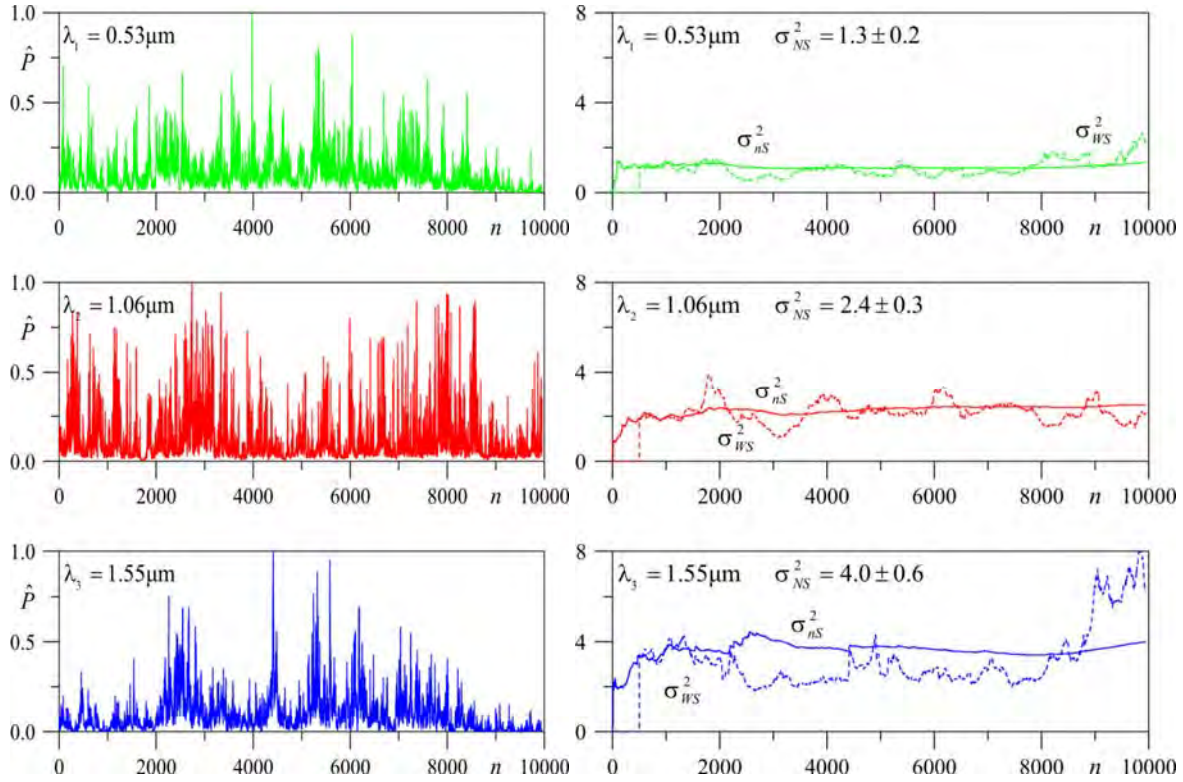


Fig. 7. Example of the received power fluctuation dynamics over 149 km propagation path (similar to as shown in Fig. 5) with strongest received power spikes at $\lambda_3 = 1.55 \mu\text{m}$ (left), and the corresponding evolution of the aperture-average scintillation indices $\sigma_{nS}^2(n)$ (solid lines) and $\sigma_{wS}^2(n)$ for $n_w = 2000$ (dashed lines).

Scintillation Index Dynamics. For analysis of temporal dynamics of the pupil-plane intensity scintillations consider computation of the normalized variance of intensity fluctuations at each pixel of the photo-array within the receiver aperture area,

$$\sigma_J^2(\mathbf{r}_m) = J^{-1} \sum_{n=1}^J [I_n(\mathbf{r}_m) - \bar{I}_J(\mathbf{r}_m)]^2 / \bar{I}_J^2(\mathbf{r}_m), \quad (1)$$

where \mathbf{r}_m is the transverse coordinate vector defining the m th pixel in the plane of the photo-array, $\{I_n(\mathbf{r}_m)\}$ ($n=1, \dots, N$) is the set of N short-exposure pupil-plane intensity distributions that are recorded with frame rate 200 fr/sec, and $\bar{I}_J(\mathbf{r}_m) = J^{-1} \sum_{n=1}^J I_n(\mathbf{r}_m)$ is an intensity distribution obtained by averaging of J subsequent frames (time-average image). Note that averaging over the set of $J=N \approx 10000$ frames in Eq. (1) is equivalent to time averaging over nearly 50 seconds. The normalized variance (1) is referred to as the scintillation index. By averaging $\sigma_J^2(\mathbf{r}_m)$ over all pixels inside the receiver aperture area we obtain the aperture-average scintillation index $\sigma_{JS}^2 = \langle \sigma_J^2(\mathbf{r}_m) \rangle_S$, where $\langle \rangle_S$ defines averaging over receiver aperture or space averaging. In order to evaluate whether the observed intensity scintillations can be considered as a stationary random process, consider temporal dynamics of the scintillation index by using either increasing number $J=n$ of subsequent frames $\sigma_{nS}^2(n)$ or “moving” (window) averaging of $J=n$ sequential frames $\sigma_{wS}^2(n, n_w)$, where n_w is a number of frames in the selected averaging window. Both $\sigma_{nS}^2(n)$ and $\sigma_{wS}^2(n)$ dependencies are shown in Fig. 7; the values σ_{nS}^2 are given inside the corresponding plots.

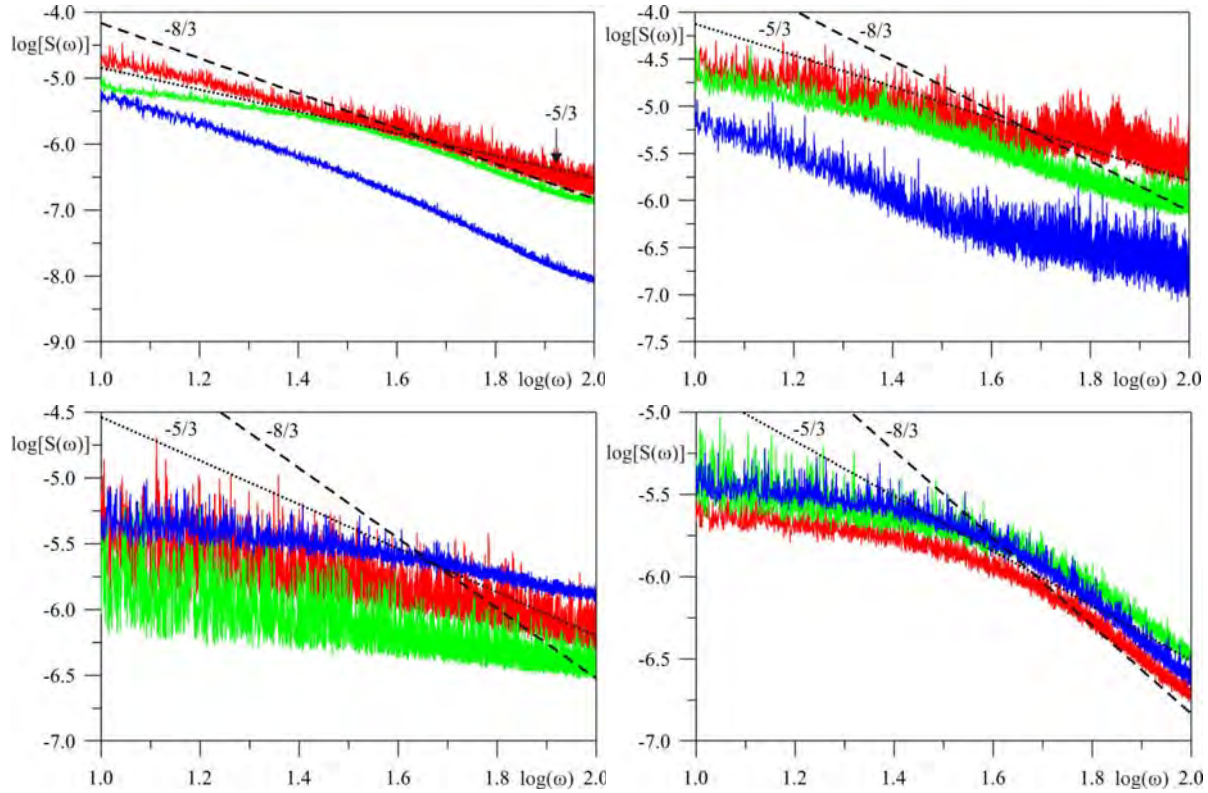


Fig. 8. Characteristic examples of temporal power spectra for pupil-plane intensity scintillations measured in the long-range COMBAT experiments for four different experimental trials. In each plot the spectra correspond to intensity scintillations simultaneously measured at three different wavelengths ($\lambda_1 = 0.53 \mu\text{m}$, $\lambda_2 = 1.06 \mu\text{m}$, and $\lambda_3 = 1.55 \mu\text{m}$). The data were taken on 02/13/10 at 7:30pm (top left), and at 10:30pm (top right), and on 02/16/10 at 9:51pm (bottom left), and on 02/17/10 at 9:05pm local time. For convenience of comparison with the temporal power spectrum of intensity fluctuations derived from the Kolmogorov theory the characteristic $-8/3$ slope of this spectrum as well as $-5/3$ slope observed in ref [2] are shown by the corresponding straight lines. The frequency ω is normalized by 1.0 Hz.

The dependences $\sigma_{NS}^2(n)$ and $\sigma_{WS}^2(n)$ characterize temporal changes of the aperture-average scintillation index occurring during the time of measurements trial. The scintillation index plots clearly indicate the statistical non-stationary character of the intensity scintillation process and strong impact of spikes in the received power. The appearance of the giant spikes results in rapid increases in the scintillation index $\sigma_{WS}^2(n, n_w)$ that makes the scintillation process highly non-stationary. In Fig. 7 this effect is more pronounced for the set of data obtained at $\lambda_3 = 1.55 \mu\text{m}$. The giant spikes also contribute to non-ergodicity of intensity scintillations. The assumption of ergodicity of the intensity scintillation statistical process can be challenged by comparing values of the scintillation indexes σ_{NS}^2 and σ_{SN}^2 that are obtained by changing the order of spatial and temporal averaging in the same experimental trial. Comparison of the corresponding values σ_{NS}^2 and σ_{SN}^2 shows that these values are quite different which makes questionable the applicability of the ergodic hypothesis [3,4].

3.4 Temporal Spectrum of Intensity Scintillations. Consider examples of a temporal power spectrum of the pupil-plane intensity fluctuations which are obtained using computer processing of the COMBAT experimental data. The aperture-average spectral density of intensity fluctuations $S(\omega)$ was defined as

$$S(\omega) = \frac{1}{M_S} \sum_{m=1}^{M_S} \left[|s_I(\omega, \mathbf{r}_m)|^2 / |s_I(\omega = 0, \mathbf{r}_m)|^2 \right], \quad (2)$$

where $s_I(\omega, \mathbf{r}_m)$ is a random realization of a temporal power spectrum corresponding to the m th pixel of the photo-array, and M_S the number of pixels used for the power spectrum computations. For each m th pixel, temporal spectra $s_I(\omega, \mathbf{r}_m)$ were calculated by taking digital Fourier transforms of the set of $N=10000$ intensity values $I_n(\mathbf{r}_m)$, where $n=1, \dots, N$. Note that the photo-array pixel corresponded to a $6.4 \times 6.4 \text{ mm}^2$ area of the receiver aperture in the long-range and $0.3 \times 0.3 \text{ mm}^2$ in the tactical-range COMBAT settings. To reduce computational time in each of N

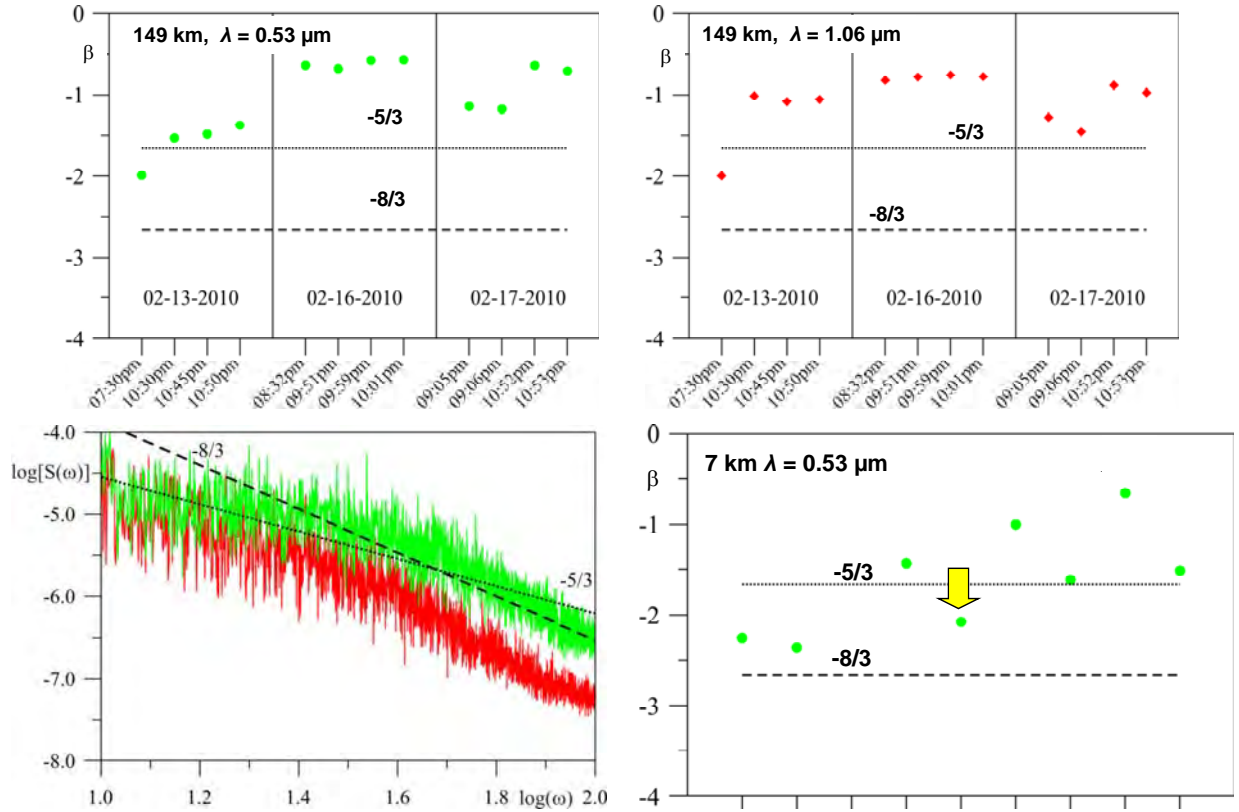


Fig. 9. Summary of pupil-plane intensity scintillations temporal power spectra analysis for long-range (top) and tactical-range (bottom) experiments. The calculated from the experimental data exponents β in the approximating spectrum power-low ω^β for different experimental trials and the example of the power spectra for 7 km propagation path (bottom left) corresponding to the experimental trial indicated by arrow.

processed frames only $M_S = 1000$ intensity values were used. The pixels \mathbf{r}_m , $m=1, \dots, M_S$, selected for computation of $s_I(\omega, \mathbf{r}_m)$ were those forming a grid with 10 pixel spacing that was centered on and covers the receiver aperture.

Four examples of the temporal power spectra obtained using COMBAT long-range data are show in Fig. 8. As can be seen from these examples the spectral functions $S(\omega)$ were changing considerably from one to another experimental data collection trial. Also note that these experimental spectra are quite different from the corresponding temporal power spectrum functions that are derived from the Kolmogorov turbulence theory and Taylor's frozen turbulence hypothesis [3,5]. These theory-based temporal power spectrum functions are essentially unchanged within the low-frequency band for $0 < \omega < \omega_0 = 2.5V_\perp / (L\lambda)^{1/2}$ and decay as $\omega^{-8/3}$ for higher frequencies [5]. Here V_\perp is a transversal component of wind velocity. The temporal power spectrum curves in Fig. 8 (except the plots at bottom right) decay with a nearly constant, and significantly different than $-8/3$, exponent β in the approximating spectrum power-law ω^β within the entire frequency band. The exponents β in the power-law ω^β approximations of the experimental temporal power spectra obtained for several COMBAT/LR experimental trials are summarized in Fig. 9 for $\lambda_1 = 0.53 \mu\text{m}$ and $\lambda_2 = 1.06 \mu\text{m}$ wavelengths. As can be seen from the data presented in Fig. 9 in most experimental trials the temporal power spectra can be approximated as ω^{-1} for both wavelengths. These results present significant deviation from the existing predictive models.

Examples of intensity fluctuation power spectrum obtained for the tactical-range distance and the values of exponent β for eight different set of measurements are correspondingly shown in bottom left and right plots in Fig. 9. Note that in this case within the low-frequency band ($\omega < \omega_0 \cong 30 \text{ Hz}$) the power spectrum is nearly constant and decays with exponent $\beta = -2.2$ at higher frequencies as theory predicts. This shape of the power spectrum is consistent with the theoretical prediction although the decay exponent is slightly larger than $-8/3$. In all tactical range experimental trails we observed shapes of spectra similar to Fig. 9 (bottom left) having decay parameters ranging between -2.5 and -1 as shown in Fig. 9 (bottom right). This deviation from theoretical (plane wave) $\omega^{-8/3}$

approximation is most likely related with violation of Taylor's frozen turbulence hypothesis that assumes constant wind velocity along the entire propagation path.

4. SUMMARY

To optimally design, build, and understand the performance of the new generation of long-range optical systems requires analysis of optical wave propagation along various atmospheric paths that may cross several extended (deep) regions of atmosphere with quite distinctive spatial structures and temporal dynamics, and quite likely, development of techniques to mitigate these effects. This analysis is currently performed using a framework of the classical "fully developed" Kolmogorov-Obukhov optical turbulence theory [6,7]. In this theory the atmosphere is described by three dimensional boundless, statistically *homogeneous and isotropic* random fields of refractive index fluctuations (atmospheric eddies). In this idealization, the impact of boundary conditions imposed by terrain, and hydro-thermodynamic processes in the atmosphere is assumed to be "forgotten" due to a cascade of energy transfer from larger to smaller scale eddies – the process that rationalizes the Kolmogorov's assumption of statistical isotropy of fully developed turbulence.

In reality, these ideal homogeneity and isotropy conditions do not exist at large scales, as they are destroyed by gravity and solar radiation induced buoyancy and friction forces that lead to formation of distinct nearly horizontally aligned atmospheric layers [8,9]. These atmospheric effects can severely impact optical wave propagation over long distances.

The results of the atmospheric characterization experiments over long- (149-km) and relatively short (7-km) paths presented allow direct comparison of atmospheric effects induced scintillations of laser beam intensity for different wavelengths. They also clearly show difficulties in interpretations of the observed long-range phenomena based solely on the classical Kolmogorov optical turbulence theory. As a path forward we can point out several future research and development directions towards better understanding physics of laser beam propagation along long-distances, including:

1. Research focused on merging statistical (Kolmogorov turbulence based) and deterministic computational fluid dynamics approaches, combined with wave optics modeling of optical wave propagation over atmospheric paths.
2. Development of mathematical and computational techniques for predictive modeling of optical wave propagation in highly anisotropic turbulence layers.
3. Development of theoretical framework numerical simulation tools that merge refractive and diffractive optics approaches.
4. Engineering of unconventional optical fields (laser beams) and optical system architectures which are less sensitive to atmospheric distortions over long propagation paths.
5. Development of unconventional adaptive beam control techniques.

We also believe that more long-range atmospheric optical propagation experiments are needed to directly associate the observed anomalies in laser beam and image characteristics with meteorological data and the results of high-performance computing of atmospheric dynamics.

5. ACKNOWLEDGEMENTS

This project was supported through the Cooperative Agreements between the US Army Research Laboratory and both the University of Dayton and Optonicus LLC.

6. REFERENCES

- [1] M. A. Vorontsov, G. W. Carhart, V. S. Rao Gudimetla, T. Weyrauch, E. Stevenson, S. L. Lachinova, L. A. Beresnev, J. Liu, K. Rehder, and J. F. Riker, "Characterization of atmospheric turbulence effects over 149 km propagation path using multi-wavelength laser beacons," in *Proceedings of the 2010 AMOS Conference*, S. Ryan, ed., p. E18 (2010).
- [2] V.V. Nosov, V.P. Lukin, E.V. Nosov, A.V. Torgaev, V.M. Grigoriev, P.G. Kovadlo, "Coherent structures in the turbulent atmosphere", *Mathematical Models of Non-linear Phenomena, Processes and Systems: From Molecular Scale to Planetary Atmosphere*. By ed. A. Nadykto et al. - N.Y.: Nova Science Publishers, Chapter 20, (2010).

- [3] V. I. Tatarskii, *Wave Propagation in a Turbulent Medium*, ser. McGraw-Hill Series in Electrical Engineering. New York: McGraw-Hill, (1961).
- [4] A. Ishimaru, *Wave Propagation and Scattering in Random Media*. New York: Academic Press, (1978).
- [5] L. C. Andrews and R. L. Phillips, *Laser Beam Propagation through Random Media*, SPIE, (1998).
- [6] A. N. Kolmogorov, "The local structure of turbulence in incompressible viscous fluid for very large Reynolds numbers," *Dokl. Akad. Nauk SSSR*, vol. 30, no. 4, pp. 299–303, 1941, [English translation in *Turbulence: Classic Papers on Statistical Theory* (ed. S. K. Friedlander and L. Topper), p. 151, Interscience, NY, (1961).
- [7] A. M. Obukhov, "On the distribution of energy in the spectrum of turbulent flow," *Dokl. Akad. Nauk SSSR*, vol. 32, no. 1, p. 22, (1941).
- [8] S. Lovejoy, A. F. Tuck, S. J. Hovde, and D. Schertzer, "Do stable atmospheric layers exist?" *Geophysical Research Letters*, vol. 35, L01802, (2008).
- [9] S. Lovejoy, A. F. Tuck, S. J. Hovde, and D. Schertzer, "Is isotropic turbulence relevant in the atmosphere?" *Geophysical Research Letters*, Vol.. 34, L15802, (2007).